Journal Pre-proof

Interfacial engineering of Bi_2MoO_6-$BaTiO_3$ Type-I heterojunction promotes cocatalyst-free piezocatalytic H_2 production

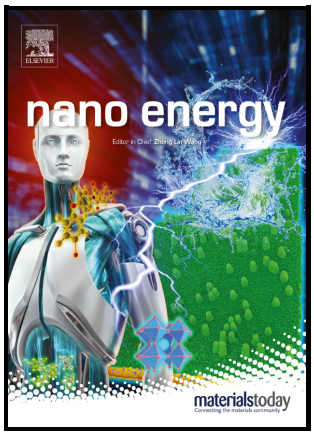

Kailai Zhang, Xiaodong Sun, Haitang Wang, Yali Ma, Hongwei Huang, Tianyi Ma

PII: S2211-2855(23)01043-1

DOI: https://doi.org/10.1016/j.nanoen.2023.109206

Reference: NANOEN109206

To appear in: *Nano Energy*

Received date: 29 October 2023
Revised date: 6 December 2023
Accepted date: 15 December 2023

Please cite this article as: Kailai Zhang, Xiaodong Sun, Haitang Wang, Yali Ma, Hongwei Huang and Tianyi Ma, Interfacial engineering of Bi_2MoO_6-$BaTiO_3$ Type-I heterojunction promotes cocatalyst-free piezocatalytic H_2 production, *Nano Energy,* (2023) doi:https://doi.org/10.1016/j.nanoen.2023.109206

Interfacial engineering of Bi_2MoO_6-$BaTiO_3$ Type-I heterojunction promotes cocatalyst-free piezocatalytic H_2 production

Kailai Zhang[a,b], Xiaodong Sun*[c], Haitang Wang[a], Yali Ma*[a], Hongwei Huang[d] and Tianyi Ma*[b]

K. Zhang, H, Wang, Dr. Y. Ma

College of Chemical Engineering, Shenyang University of Chemical Technology, Shenyang 110142, P. R. China

Email: mayalichem@126.com

K. Zhang, Prof. T. Ma

School of Science, RMIT University, Melbourne, VIC 3000, Australia

E-mail: tianyi.ma@rmit.edu.au

Dr. X. Sun

Institute of Clean Energy Chemistry, Key Laboratory for Green Synthesis and Preparative Chemistry of Adv. Mater., College of Chemistry, Liaoning University, Shenyang 110036, People's Republic of China

E-mail: sunxiaodong@lnu.edu.cn

Prof. H. Huang

Beijing Key Laboratory of Materials Utilization of Nonmetallic Minerals and Solid Wastes, National Laboratory of Mineral Materials, School of Materials Science and Technology, China University of Geosciences, Beijing, 100083, China

Abstract

Single component semiconductor materials with piezoelectric response can promote the activation of hydrogen ions (H^+) and the generation of hydrogen (H_2) under the action of mechanical force, but the high recombination rate of carriers is the major obstacle to strengthen piezocatalytic efficiency. Here, a groundbreaking Bi_2MoO_6-$BaTiO_3$ (BMO-BTO) Type-I heterojunction piezocatalyst is successfully fabricated through a solvothermal strategy, and applied for cocatalysts-free piezocatalytic H_2 production reaction. Under ultrasonic vibration, the H_2 production rate of BMO-0.1BTO heterojunction can reach up to nearly 152.57 μmol/g/h, which is approximately 9.33 and 4.47 times with respect to that of pristine BMO (16.36 μmol/g/h) and BTO (34.16 μmol/g/h) alone, respectively. Furthermore, BMO is also combined

with other commonly used piezocatalysts to construct heterojunctions, and analogous marvelous piezocatalytic H_2 production performance was attained. The enhanced piezocatalytic H_2 production performance can be credited to the established built-in electric field (BIEF) in heterojunction extraordinarily suppressed the recombination rates of piezocarriers, rather than an increase in piezoelectricity, which is emphatically verified through a series of physics and chemical characterizations. This study presents an innovative paradigm for fabricating BMO-based heterojunction piezocatalyst to efficiently convert mechanical energy into chemical energy.

Keywords:

Piezocatalysis, Hydrogen production, Type-I heterojunction, Carriers separation

1. Introduction

Currently, addressing the escalating energy demand and associated environmental issues necessitates the substitution of conventional fossil fuels with renewable energy sources[1-4]. Hydrogen (H_2) energy holds immense promise as a sustainable energy source due to its efficient combustion, abundant reserves not reliant on fossil fuels, high energy content, minimal consumption, non-toxicity, lack of pollution, and high utilization rate, but the challenge of achieving environmentally friendly, convenient, and cost-effective H_2 production remains a significant issue[5-7]. Photocatalytic materials have been extensively studied for their ability to harness light energy to generate H_2, as documented in numerous scientific publications. Nevertheless, challenges such as limited responsiveness to visible light, high recombination rates of carriers, and the absence of activity sites hinder the widespread implementation of photocatalytic technology[8-12]. Furthermore, an alternative approach to catalytic H_2 production, known as the electrocatalytic H_2 production process, not only demands a significant

amount of electrical energy, but also yields products with poor economic viability, thus limiting its widespread adoption[13-16].

Piezocatalytic H_2 production process offers the potential to significantly lower catalysis expenses by harnessing secondary energy sources like ambient mechanical energy, and it does not rely on light activation[17-22]. When a piezocatalytic material experiences an external mechanical force, its inherent polarization properties result in the generation of built-in electric field (BIEF). Consequently, under the influence of BIEF, carriers within the material separate in opposite directions and eventually accumulate at different surface sites. Once the carriers are efficiently separated, they can drive the reduction reaction for H_2 production. This innovative approach for transforming mechanical energy into chemical energy may serve as a novel alternative technique for producing H_2[23-27]. In order to drive the piezocatalytic H_2 production reaction, the most important thing is the selection of suitable piezocatalysts. It is essential to note that the piezoelectric effect can only occur in non-centrosymmetric crystals. In recent times, piezoelectric materials such as ZnO, transition metal dihalides, g-C_3N_4, metal Organic Frameworks (MOFs) and Bismuth-based (Bi-based) oxide semiconductor catalysts have shown promise in efficiently generating H_2 from water[28-35]. Among them, the mismatch of lattices between cations caused by the low tolerance factor of endows Bi-based oxides with a significant level of spontaneous polarization and a high piezoelectric coefficient at room temperature. Consequently, these materials have emerged as a highly desirable catalyst for piezocatalytic H_2 production. Nonetheless, the high recombination rate of piezocarriers hampers the widespread utilization of Bi-based piezocatalytic materials on a large scale. Therefore, it is highly significant to explore suitable strategies for enhancing the piezocatalytic H_2 production performance of Bi-based piezocatalytic materials. Currently, various strategies are employed to improve the piezocatalytic H_2 production performance of Bi-based piezocatalysts. These strategies include crystal face engineering, co-catalyst engineering and

heterojunction construction, among which the most effective strategy is the heterojunction construction[34, 36]. The numerous researches have demonstrated that the photocatalytic H_2 production performance can be substantially enhanced through the integration of two or more photocatalysts into semiconductor heterojunctions[37-39]. This effect primarily arises from the creation of a BIEF within the heterojunctions, which can be utilized as a driving force to effectively mitigate the recombination rate between photo-generated carriers. Due to the analogous roles that carriers play in facilitating redox reactions during both piezocatalysis and photocatalysis, the utilization of two distinct piezoelectric materials to fabricate polar heterojunctions can also create a new BIEF. Consequently, this BIEF enables efficient separation and transfer of piezocarriers, which ultimately results in the improved piezocatalytic efficiency for the H_2 production reaction. Bismuth molybdate (Bi_2MoO_6, BMO), as a high-efficient bismuth-based catalyst, has shown obvious advantages in the realm of photocatalytic H_2 production owing to its strong visible light response, high tunability, remarkable stability and eco-friendly attributes[40]. Due to the similar behavior between piezocatalysis and photocatalysis, it is expected that BMO-based materials will be applied into piezocatalysis to achieve H_2 production reaction. Lamentably, the literature on piezocatalytic H_2 production of BMO-based materials has not been reported. Considering the benefits of BMO-based materials and the limited research in the field of piezocatalytic H_2 production, it is valuable to deeper delve into this subject.

Hence, in this work, we utilized BMO as a representative example of a high-performance Bi-based piezocatalyst to combine with Barium titanate ($BaTiO_3$, BTO) possessing exceptional piezoelectricity and well-matched energy band structure to fabricate Bi_2MoO_6-$BaTiO_3$ (BMO-BTO) Type-I heterojunctions. It is reported that BMO-BTO heterojunctions can be used in piezocatalytic H_2 production reaction driven by mechanical energy for the first time. Piezocatalytic H_2 production reaction and piezoelectric response force microscope (PFM)

characterization provided strong evidence for BMO-BTO heterojunctions to establish BIEF to drive the migration of piezocarriers under ultrasonic vibration. Moreover, BMO was utilized in combination with other various conventional piezoelectric semiconductor materials to create heterojunctions, which triggered similarly excellent piezocatalytic H_2 production performance. Ultimately, a novel piezocatalytic H_2 production mechanism of BMO-BTO Type-I heterojunctions had been put forward.

2. Experimental section

2.1 Materials and reagents

Ethylene Glycol (EG), Methanol (MeOH), Ethanol (EtOH), Barium titanate (BTO), Cadmium sulfide (CdS), Zinc oxide (ZnO), Strontium titanate (STO), $Bi(NO_3)_3 \cdot 5H_2O$ and $Na_2MoO_4 \cdot 2H_2O$ were purchased from Shanghai Aladdin Bio-chemical Technology Co. , Ltd. Microcrystalline cellulose (MCC) was purchased from Bide medical technology Co., ltd. All chemical reagents were of analytical grade and used without further purification. High purity nitrogen (N_2) (99.999 %) was purchased from Shenyang gas cylinder factory.

2.2. Preparation of piezocatalysts

2.2.1 Preparation of BMO

Bismuth molybdate (Bi_2MoO_6 abbreviated as BMO) piezocatalyst was synthesized by simply modifying the synthesis method of BMO reported in previous literatures[41]. In typical, 970 mg of $Bi(NO_3)_3 \cdot 5H_2O$ was accurately weighed and stirred at room temperature at 600 r/min for 1 h to completely dissolve in 40 mL of EG. Subsequently, 240 mg of $Na_2MoO_4 \cdot 2H_2O$ and 10 mL of EtOH were added, and continued to stir for 1 h until $Na_2MoO_4 \cdot 2H_2O$ was completely dissolved. Then the obtained mixed solution was sealed into a 100 mL stainless steel reactor and reacted at 190 ℃ for 2 h. After the reaction was stopped, the solution was centrifuged to obtain a solid, then washed with EtOH for 6 times by means of high-speed centrifugation, and then dried at 70 ℃ for 24 h. The resulting yellowish product was named BMO.

2.2.2 Preparation of BMO-piezoelectric semiconductor heterojunctions

The preparation method of BMO-BTO heterojunctions was similar to that of BMO. Specifically, 970 mg of $Bi(NO_3)_3 \cdot 5H_2O$ was accurately weighed and stirred at room temperature at 800 r/min for 1 h to completely dissolve in 40 mL of EG. Then 100 mg of BTO was added and stirred for another 2 h to mix well. Subsequently, 240 mg of $Na_2MoO_4 \cdot 2H_2O$ and 10 mL of EtOH were added to the above mixture, and the mixed solution was stirred for 60 min until $Na_2MoO_4 \cdot 2H_2O$ was completely dissolved. Then the obtained mixed solution was sealed into a 100 mL stainless steel reactor and reacted at 190 ℃ for 2 h. After the reaction was stopped, the solution was centrifuged to obtain a solid, washed with EtOH for 6 times by means of high-speed centrifugation, and then dried at 70 ℃ for 12 h. The resulting product was denoted as BMO-0.1BTO heterojunction. BMO-0.05BTO and BMO-0.2BTO heterojunction were simply prepared except for changing the added amount of BTO to 50 mg and 200 mg, respectively. The preparation methods of BMO-0.1CdS, BMO-0.1MCC, BMO-0.1ZnO and BMO-0.1STO heterojunctions were similar to those of BMO-0.1BTO heterojunction with the only difference being the substitution of 100 mg of BTO with 100 mg of CdS, MCC, ZnO and STO, respectively.

2.3 Characterizations

Powder X-ray diffraction (XRD, Bruker D8) was utilized to investigate the crystal structure information piezocatalysts. Scanning electron microscopy (SEM, SUPRA55, ZEISS, Germany) and transmission electron microscopy (TEM, JEM-2100F, JEOL, Japan) were utilized for the examination of the morphology of piezocatalysts. The chemical state of piezocatalysts was studied using X-ray photoelectron spectroscopy (XPS, ESCALAB 250Xi, Thermo fisher). The Fourier transform infrared spectroscopy (FTIR) images were carried out to obtain the surface functional group information of the piezocatalysts using NICOLET IS10 (Thermo Fisher) spectrophotometer. The piezoelectric properties of piezocatalysts were analyzed by piezoelectric force microscopy (PFM) with Bruker Multimode 8. Thermogravimetric (TG) was

carried out to obtain the thermal stability information of piezocatalysts using METTLER TOLEDOTGA/SDTA851 instrument.

2.4 Electrochemical tests

The electrochemical impedance spectroscopy (EIS) Nyquist plots, Mott-Schottky (M-S) curves and piezocurrent data were acquired using an electrochemical workstation (CHI760E) in the presence of a 0.2 M Na_2SO_4 electrolyte solution. Pt was employed as the counter electrode, while Ag/AgCl was employed as the reference electrode. Except for piezoelectric current characterization, which is conducted under ultrasonic conditions, all other electrochemical characterizations are performed under normal conditions. The ultrasonic frequency and power are set to 50 kHz and 300 W, respectively.

2.5 Experimental procedure

The piezocatalytic H_2 production performances of samples were measured using an ultrasonic cleaner (Kunshan Ultrasonic Instrument Co. Ltd.) with various power levels (180 W, 240 W, and 300 W). To minimize the impact of temperature variations, the reaction system was kept at a constant temperature of 26 °C ± 1 °C via circulating water. Normally, in a sealed Pyrex reactor having an overall capacity of 300 mL, 50 mg of piezocatalyst was introduced in 200 mL of a deionized water/methanol (MeOH) mixture (10 vol% MeOH). Afterwards, the Pyrex reactor was evacuated to remove air with N_2 for 1 h. No additional co-catalysts were employed in the piezocatalytic reaction. Afterwards, the Pyrex reactor was subjected to piezocatalysis by exposing it to an ultrasonic cleaner. To quantify the concentration of H_2, a 1000 μL sample of the gas mixture was obtained from Pyrex reactor after reacting for 2 h, which was then introduced into a gas chromatograph for determination (GC-9790, Fu Li, China).

3. Results and discussion

3.1 Catalyst synthesis and characterization

Firstly, BMO and BMO-BTO heterojunction piezocatalysts were fabricated through a

solvothermal strategy (190 ℃, 2 h) in a mixed solvent system of ethanol/ethylene glycol (EtOH/EG), respectively (Fig. 1a). As a rule, BTO exhibits different crystal structures at different temperatures. Above 120 ℃, BTO exists in a paraelectric phase with a space group of Pm3m and without piezoelectric characteristics. At exactly 120 ℃, a paraelectric-ferroelectric phase transition occurs and BTO enters the ferroelectric phase, where the space group becomes P4mm, and spontaneous polarization occurs along the quadruple axis, leading to the development of spontaneous polarization and piezoelectric characteristics. At 5 ℃, another ferroelectric-ferroelectric phase transition occurs, BTO assumes the Amm2 space group, and spontaneous polarization arises along the double axis. At -9 ℃, another ferroelectric-ferroelectric phase transition occurs, with BTO adopting the R3m space group and spontaneous polarization occurring along the triple axis. Therefore, in the solvothermal reaction at 190 ℃, BTO will undergo a phase transition that can be gradually recovered with the decrease in temperature. Consequently, it is assumed that the piezoelectric phase of BTO remains unaffected after cooling to room temperature. Fig. S1-S5 showed the macroscopic topography of the prepared samples.

To validate the successful construction of heterojunction, the microstructure of piezocatalytic material was firstly analyzed by scanning electron microscope (SEM) and transmission electron microscopy (TEM). Firstly, in Fig. 1b, SEM image of BMO showed the morphology of three-dimensional microspheres formed by nanosheets. Moreover, SEM images of BMO-0.05BTO, BMO-0.1BTO and BMO-0.2BTO heterojunction were displayed in Fig. 1c and Fig. S6. It is evident that the microstructure of BMO-BTO heterojunction was basically consistent with that of BMO microspheres, which may be because BTO was covered by BMO. Finally, Fig. 1d-e exhibited the TEM images of BMO and BMO-0.1BTO heterojunction. BMO still presented microspheres morphology composed of nanosheets, while the TEM images of BMO-0.1BTO heterojunction further suggested that the morphology of BMO and BMO-

0.1BTO heterojunction seemed the same, which indicated that BTO existed inner BMO. In the meantime, the energy dispersive X-ray (EDX) spectroscopy element mapping images further showed five elements, Bi, Mo, O, Ba and Ti were distributed on the BMO-0.1BTO heterojunction (Fig. 1f-j), which indicate the presence of BTO in the constructed heterojunction. Moreover, the analysis of SEM and EDX elemental spectroscopy mapping images confirmed the successful fabrication of other heterojunctions (Fig. S7-S14).

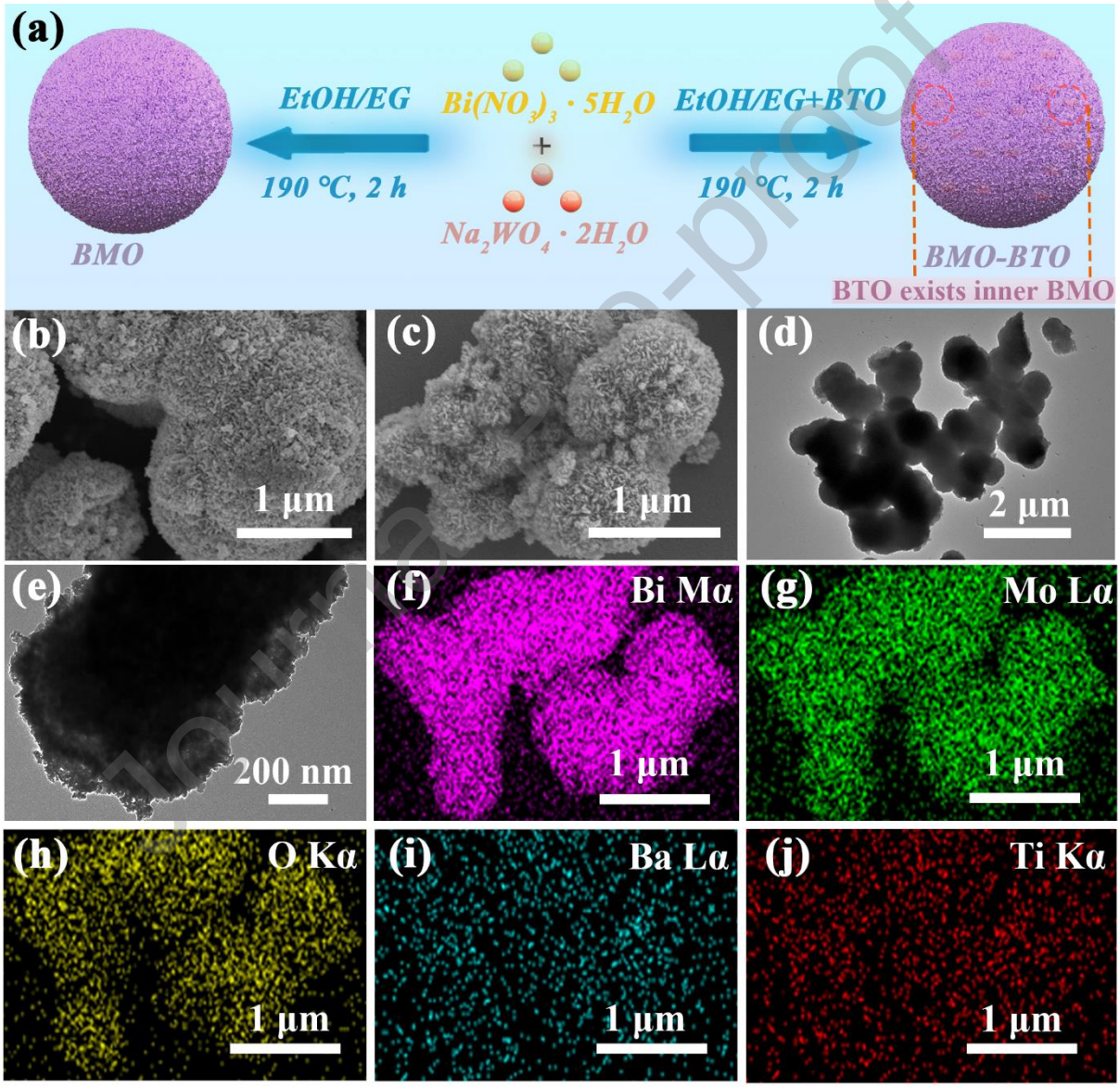

Fig. 1. (a) Schematic illustration for the facile sythesis pathway of BMO and BMO-BTO heterojunctions. (b-c) SEM images of BMO and BMO-0.1BTO heterojunction. (d-e) TEM images of BMO and BMO-0.1BTO heterojunction. (f-j) EDX elemental mapping images (Bi Mα, Mo Lα, O Kα, Ba Lα and Ti Kα) of BMO-

0.1BTO heterojunction.

Powder X-ray diffraction (PXRD) analysis was performed to further prove the successful combination of BMO and BTO (Fig. 2a). For the BMO, the diffraction peaks observed at 2θ of 11.88°, 23.52°, 28.24°, 34.40°, 36.01°, 39.54°, 46.71°, 55.45°, 58.42°, 68.28°, 75.39° and 77.99° could be perfectly attributed to the (020), (111), (131), (220), (151), (240), (202), (331), (262), (004), (333) and (064) planes of orthorhomeric phase BMO (JCPDS No. 76-2388)[42]. Also, for BTO, the peaks observed at 2θ of 22.25°, 31.48°, 31.64°, 38.89°, 44.90°, 45.38°, 55.97°, 56.28°, 65.75°, 74.39°, 79.44° and 83.50° could be well assigned to the (100), (101), (110), (111), (002), (200), (112), (211), (202), (103), (311) and (222) planes of tetragonal phase BTO (JCPDS NO.75-0460). Noticeably, the diffraction peaks of BTO and BMO exhibited a relatively high intensity, which indicated that both prepared BMO and purchased commercial BTO had good crystallinity. In addition, for the BMO-0.05BTO, BMO-0.1BTO and BMO-0.2BTO heterojunction, as expected, apart from the typical diffraction peaks assigned to BMO, the typical diffraction peaks observed at 2θ of 22.25°, 31.48°, 38.89°, 44.90°, 45.38°, 55.97°, 56.28° and 65.75° were in perfect agreement with the (100), (101), (111), (002), (200), (112), (211) and (202) planes of BTO (JCPDS NO.75-0460), and the intensity of the diffraction peaks increased as the loading amount of BTO increased. These results unambiguously validated that BTO nanoparticles had been successfully combined with BMO microspheres by solvothermal reaction. Furthermore, PXRD analysis was conducted to provide further evidence of the successful integration of MCC, ZnO, STO, or CdS with BMO (Fig. S15-S18). For the BMO-0.1MCC heterojunction, typical diffraction peaks attributed to BMO were observed, but no typical diffraction peaks were observed at 2θ of 14.9°, 16.4°, and 22.8°, which correspond to the $(1\bar{1}0)$, (110), and (200) crystal planes of the non-centrosymmetric MCC. This may be due to the low intensity of the MCC diffraction peaks or the small sample loading. In addition, for the BMO-0.1ZnO heterojunction, as expected, as expected, apart from the typical diffraction

peaks assigned to BMO, the typical diffraction peak observed at 2θ of 31.77° was in perfect agreement with the (100) plane of hexagonal phase ZnO (JCPDS NO.36-1451). Furthermore, for the BMO-0.1STO heterojunction, apart from the typical diffraction peaks assigned to BMO, the typical diffraction peak observed at 2θ of 39.98° was in perfect agreement with the (111) plane of cubic phase STO (JCPDS No. 35-0734). Finally, for the BMO-0.1CdS heterojunction, as expected, apart from the typical diffraction peaks assigned to BMO, the typical diffraction peaks observed at 2θ of 30.63°, and 43.87° were in perfect agreement with the (200) and (220) planes of cubic phase CdS (JCPDS No. 65-2887). These results confirmed that MCC, ZnO, STO, or CdS had been successfully combined with BMO microspheres via a solvothermal reaction. The elemental composition and chemical states of samples were further analyzed by X-ray photoelectron spectroscopy (XPS) measurements. The XPS survey spectrum (Fig. 2b) revealed the presence of Bi, Mo and O elements in BMO. And Ba, Ti and O elements existed in BTO. Additionally, BMO-0.1BTO heterojunction exhibited the existence of Bi, Mo, O and Ba elements. Accidently, Ti element was not detected in BMO-0.1BTO heterojunction, which may be because the content of Ti element in BMO-0.1BTO heterojunction was lower than the detection limit of XPS instrument. Of course, it may also be the reason that the binding energy positions of Ti 2p and Bi 4d overlapped in the BMO-0.1BTO heterojunction. In addition, because BTO was encapsulated in the form of particles and exists inner BMO microspheres, in the detection process of XPS, X-ray may not be able to fully irradiate BTO in the BMO-0.1BTO heterojunction, thus weakening the detection signal of electronic kinetic energy. As displayed in Bi 4f XPS spectrum belonging to BMO (Fig. 2c), two strong peaks appearing at the binding energies of 164.57 and 159.26 eV can well correspond to the Bi $4f_{5/2}$ and Bi $4f_{7/2}$, respectively, which manifested that the valence state of Bi element in BMO is +3[43]. Moreover, in the Bi 4f XPS spectrum of BMO-0.1BTO heterojunction, the binding energy attributed to Bi $4f_{5/2}$ and Bi $4f_{7/2}$ of Bi^{3+} reduced to 164.25 and 158.94 eV[44]. Fig. 2d showed that two strong peaks

belonging to Mo 3d located at 235.18 and 232.19 eV in BMO could correspond to Mo $3d_{5/2}$ and Mo $3d_{7/2}$ of Mo^{6+}, respectively. In comparison to pure BMO, the peak positions of Mo $3d_{5/2}$ and Mo $3d_{7/2}$ belonging to Mo 3d in the BMO-0.1BTO heterojunction shifted to 235.07 and 232.09 eV, respectively[44]. Fig. 2e exhibited the Ba 3d XPS spectrum of BTO, where 778.2 and 793.5 eV belonged to the $3d_{5/2}$ and $3d_{3/2}$ orbits of Ba 3d, respectively. Compared with pure BTO, the two strong peaks of the $3d_{5/2}$ and $3d_{3/2}$ orbits of Ba 3d in the BMO-0.1BTO heterojunction shifted, which were 777.8 and 793.7 eV, respectively[45]. Fig. 2f showed the Ti 2P XPS spectrum of the BTO and BMO-0.1BTO heterojunction. The two peaks located at 457.7 and 463.2 eV were the $2p_{3/2}$ and $2p_{1/2}$ splitting peaks of the Ti 2p orbit in BTO, respectively[46, 47]. Conspicuously, the peaks attributed to Ti 2p of BTO were not detected, but the peaks assigned to Bi 4d of BMO were observed in the BMO-0.1BTO heterojunction. This was because Ti has a relatively low electron binding energy, and detecting Ti with XPS requires high-energy X-ray sources and sensitive detectors. If the concentration of Ti is very low, or if the XPS instrument is not optimized for the detection of Ti, it may not be detected. In addition to this, XPS is a surface-sensitive technology, which means that it mainly probes the outermost atomic layer of the material. If Ti is buried several layers below other elements or materials in the heterojunction, photoelectrons from Ti may not escape from the surface of the sample and therefore cannot be detected by the XPS instrument. And most importantly, the binding energy positions of Ti 2p and Bi 4d are highly coincident, so the high intensity peak of Bi 4d may cover up the peak belonging to Ti 2p. In addition, when compared to the binding energy positions of Mo 3d and Bi 4f in BMO, those in BMO-0.1BTO heterojunction shifted towards lower binding energy positions, which further confirmed the successful formation of the BMO-0.1BTO heterojunction. Moreover, XPS measurements were also conducted to verify the successful formation of other heterojunctions (Fig. S19-S27). The XPS analysis revealed that the BMO-0.1ZnO heterojunction comprised Bi, Mo, O and Zn elements, with Zn also displaying a

positive divalent valence. In contrast, the BMO-0.1STO heterojunction was composed of Bi, Mo, O and Sr elements, with Sr exhibiting a positive divalent state. Ti element was not observed due to the overlap of Ti 2p and Bi 4d spectral peaks. Additionally, the BMO-0.1CdS heterojunction included Bi, Mo, O and Cd, where Cd assumed a positive divalent state. The presence of S element was not detected owing to overlap of S 2p and Bi 4d spectral peaks.

Furthermore, the successful combination of BMO and BTO was further confirmed through Fourier transform infrared (FT-IR) spectroscopy. As depicted in Fig. S28, two peaks located at 3424 cm^{-1} corresponded to the O-H stretching vibrations of adsorbed water in BMO, respectively[48]. Moreover, the peak located at 841 cm^{-1} can be indicated as Mo-O stretching vibration in BMO, and the peak located at 735 cm^{-1} can be assigned to the asymmetric stretching vibration of MoO_6 in BMO[48, 49]. Additionally, the peak of 568 cm^{-1} can be regarded as the bending vibration of the Mo-O-Bi bond of Mo-O octahedron in BMO, while the absorption band in the range of 429-631 cm^{-1} represented the stretching vibration of Bi-O bond in BMO[50]. Notably, no any peaks belonging to BTO were observed, possibly because the FT-IR spectroscopy is sensitive to the concentration of the compounds being analyzed. Because the amount of BTO in the BMO-0.1BTO heterojunction was very low compared to BMO, its spectral signature may not be detectable. Moreover, because the peaks at 520-560 cm^{-1} assigned to Ti-O stretching vibration in BTO overlapped with the peaks of Bi-O bond stretching vibration in BMO (429-631 cm^{-1}), this was also an important reason why no peaks belonging to BTO can be found in the FT-IR spectroscopy of BMO-0.1BTO heterojunction. However, compared with BMO, the BMO-0.1BTO heterojunction had weaker Mo-O bond and Bi-O bond vibration, and the peak position had shifted to a certain extent, which indirectly evidenced that tight heterojunction had been formed between BTO and BMO, and eventually confirmed the successful synthesis of the BMO-0.1BTO heterojunction. Moreover, FT-IR measurements were also conducted to verify the successful formation of other heterojunctions (Fig. S29-S32).

Typically, the strong peaks in the BMO spectrum between 1000 and 600 cm^{-1}, characteristic of metal-oxygen bonds, seemed to have reduced intensity in the FT-IR spectrum of BMO-0.1MCC, BMO-0.1STO, BMO-0.1ZnO and BMO-0.1CdS heterojunctions, suggesting that BMO interacted with MCC or STO or ZnO or CdS, which may indicate the successful formation of these heterojunction materials.

Then, as exhibited in Fig. S33-S34, the thermal stability of BMO and BMO-0.1BTO heterojunction was further analyzed by thermogravimetric (TG) characterization. The TG and corresponding derivative thermogravimetric (DTG) results illustrated that the thermal decomposition reaction of BMO may require relatively high temperature to occur. As a result, the temperature change from 25 to 800 ℃ was minimal. Furthermore, the TG curves of BMO-0.1BTO heterojunction and BMO exhibited minimal differences. This may be because BMO and BTO were both relatively stable semiconductor piezocatalytic materials, and their thermal stability was similar, which finally resulted in little difference in TG curves. Except for the previous reason, the BTO content in BMO-0.1BTO heterojunction was also relatively low, and its effect may not be enough to cause a noticeable change in the TG curve.

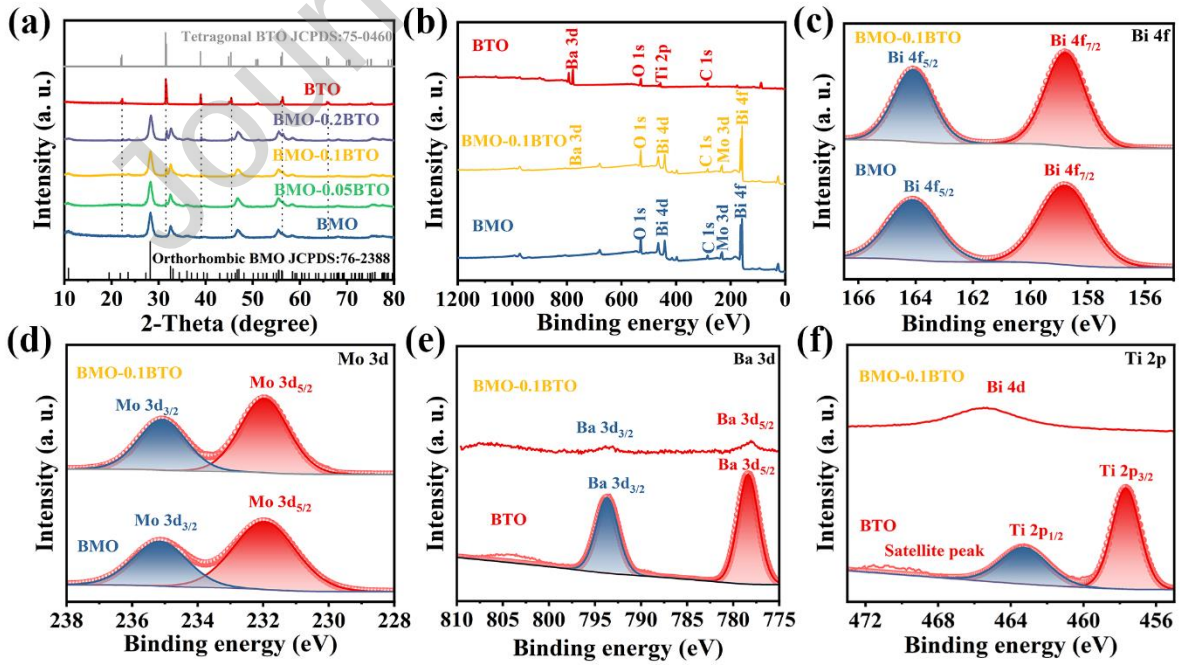

Fig. 2. (a) PXRD pattern and (b) XPS survey spectrum of BMO, BTO and BMO-0.1BTO heterojunction. (c-

d) High resoultion Bi 4f and Mo 3d XPS spectrum of BMO and BMO-0.1BTO heterojunction. (e-f) High resoultion Ba 3d and Ti 2p XPS spectrum of BTO and BMO-0.1BTO heterojunction.

3.2 Piezocatalytic H_2 production

The piezocatalytic H_2 production performances of piezocatalysts were evaluated in N_2-saturated water system, using MeOH as a sacrificial agent, without the addition of any co-catalyst. As depicted in Fig. 3a, under ultrasonic vibration, the piezocatalytic H_2 production rates of BMO and BTO were only 16.36 and 34.16 μmol/g/h, respectively. As expected, the piezocatalytic H_2 production rate substantially increased after the BMO-BTO heterojunctions were constructed. The piezocatalytic H_2 production rates of BMO-0.1BTO heterojunction, BMO-0.05BTO heterojunction and BMO-0.2BTO heterojunction can reach up to 152.57, 130.63 and 76.89 μmol/g/h, respectively. Noticablly, the mass fraction of BTO in the BMO-BTO heterojunctions and its catalytic performance for H_2 production exhibited a volcanic trend (Fig. S35). The piezocatalytic H_2 production rate of BMO-0.1BTO heterojunction with optimal BTO loading amount was nearly 9.33 and 4.47 times higher than that of pristine BMO or BTO alone. This was mainly because the new BIEF formed between the BMO and BTO guided the motion direction of piezocarriers, significantly accelerating the separation and transfer efficiency of piezocarriers. Furthormore, to exclude the effect of MeOH self-producing H_2 performance, corresponding blank controls experiments were conducted. In Fig. S36, it is shown that without the presence of the piezocatalyst, an MeOH/H_2O solution subjected to ultrasonic vibration produced a H_2 rate of 0.53 μmol/h. Merely, when BMO-0.1BTO heterojunction was added into the above MeOH/H_2O system, the H_2 production rate increased from 0.53 to 7.63 μmol/h. What's more, the piezocatalytic H_2 production rates of BMO-0.1BTO heterojunction under various ultrasonic powers were carried out. As depicted in Fig. 3b, with the gradual increase of power from 180 W to 240 W and further to 300 W, the H_2 production rates of BMO-0.1BTO heterojunction also displayed a gradual increase trend, from 32.33 to

72.56 μmol/g/h, and eventually increased to 152.57 μmol/g/h. The H_2 production rate of BMO-0.1BTO heterojunction at 300 W was about 4.71 and 2.10 times than that of 180 and 240 W, respectively. The enhanced piezocatalytic H_2 production performacne can be assigned to the higher power applied to the BMO-0.1BTO heterojunction leads to greater mechanical forces acting on the material, increasing the perturbation of the crystal lattice, resulting in a stronger BIEF to generate, which in turn accelerates the separation and transfer of piezocarriers. In addition, we studied the piezocatalytic H_2 production performance of BMO-0.1BTO heterojunction at different ultrasonic frequencies. The results were shown in Fig. S37. It is worth mentioning that at the frequency of 99 kHz, the H_2 production rate reached the maximum of 451.03 μmol/g/h. This may be because only when the applied frequency is close to the resonant frequency of the material can the most piezoelectric current be generated in the piezoelectric material to participate in the reaction, and finally the piezocatalytic performance can be improved. Considering practical applications, the piezocatalytic H_2 production performacne of BMO-0.1BTO heterojunction was examined in natural seawater. As depicted in Fig. S38, the piezocatalytic H_2 production rates of deionized and natural seawater system can reach up to 152.57 and 140.75 μmol/g/h, respectively. The observation of a slightly reduced piezocatalytic H_2 production performance of the BMO-0.1BTO heterojunction in natural seawater system indicated its wide applicability under various water quality conditions, highlighting its potential for practical use in piezocatalytic H_2 production technologies. Additionally, the stability of BMO-0.1BTO heterojunction was evaluated in detail using cyclic piezocatalytic H_2 production experiments. After 3 cycles, the H_2 production rates of the BMO-0.1BTO heterojunction slightly decreased, evidencing remarkablely piezocatalytic stability (Fig. 3c). In addition, different BMO/piezoelectric semiconductor heterojunctions were synthesized to explore the universality of BMO combined with other piezoelectric materials to enhance the piezocatalytic H_2 production performance. Not surprisingly, when BMO formed a

heterojunctions with these traditional piezoelectric semiconductor catalytic materials, the piezocatalytic H_2 production performance was also significantly improved (Fig. 3d).

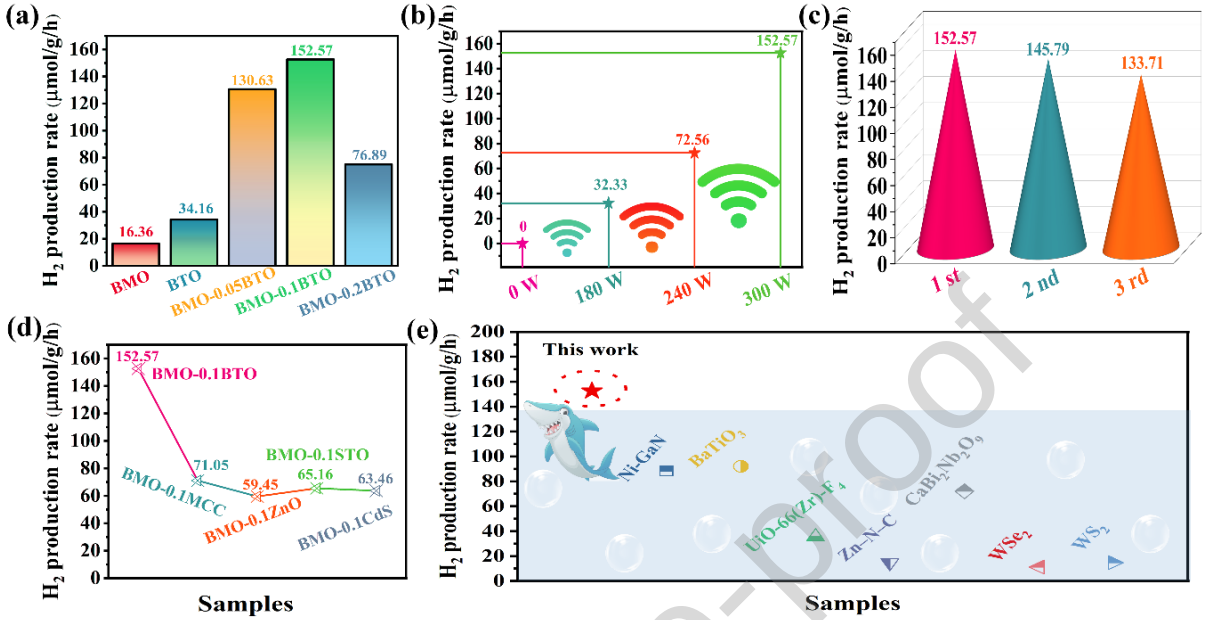

Fig. 3. (a) Piezocatalytic H_2 production rates by BMO-BTO heterojunctions with different mass fraction of BTO. (b) H_2 production rates of BMO-0.1BTO heterojunction under ultrasound vibration with different powers (180 W, 240 W and 300 W). (c) Cyclic stability of H_2 production rates under ultrasound vibration over BMO-0.1BTO heterojunction. (d) Piezocatalytic H_2 production rates by different BMO-piezocatalyst heterojunctions. (e) Piezocatalytic H_2 production rates comparison of BMO-0.1BTO heterojunction with previous reported piezocatatic materials.

To be specific, the piezocatalytic H_2 production rates of BMO-0.1MCC heterojunction, BMO-0.1ZnO heterojunction, BMO-0.1STO heterojunction and BMO-0.1CdS heterojunction can reach up to 71.05, 59.45, 65.16 and 63.46 μmol/g/h, respectively, which was 4.34, 3.63, 3.98 and 3.87 times than that of BMO, respectively. These results illustrated that it is common for BMO and semiconductor piezocatalysts to form heterojunctions to enhance the piezocatalytic H_2 production performance of BMO. Additionally, the piezocatalytic H_2 production rate of the BMO-0.1BTO heterojunction also exceeded the piezocatalytic H_2 production performance of most previously reported piezocatalytic materials (Fig. 3e and Table

S1).

3.3 Piezocatalytic Mechanism Investigation

Whether the material has piezoelectric response is a prerequisite for the occurrence of piezocatalytic reaction, so the piezoelectric properties of materials were firstly studied by piezoresponse force microscopy (PFM) measurements. Fig. 4a illustrated a schematic diagram of PFM testing the piezoelectric properties of piezoelectric materials. The testing principle of PFM is to use piezoelectric materials to precisely control the position of the sharp probe tip or scanning probe microscope tip when it interacts with the surface of the sample. When the tip is close to the surface, the piezoelectric material is mechanically deformed by the interaction between the tip and the sample. When the tip of the probe is scanned on the surface of the sample while maintaining a constant force or distance from the surface, the feedback mechanism records changes in the position of the tip of the probe. These position changes are then used to generate images of the sample surface with extremely high resolution.

As depicted in Fig. 4b and Fig. S39, the observed butterfly amplitude loop under a reverse electric field reveals the remarkable piezoelectric properties of the BMO and BMO-0.1BTO heterojunction. At the same time, according to the hysteresis loop measured by PFM, the direct current (DC) bias field from -10 to 10 V was applied, and the angle of phase hysteresis loop changes nearly 180°, which proved excellent switching polarization ability of BMO and BMO-0.1BTO heterojunction (Fig. 4c and Fig. S40).

The piezoelectric potential (V_p) of the piezoelectric materials can be accurately determined via equation 1[35]:

$$V_P = \frac{w_3 T_3 d_{33}}{\varepsilon_0 \varepsilon_r} \quad (1)$$

Where, T_3 is the stress perpendicular to the piezocatalyst, W_3 is the thickness of the piezocatalyst, d_{33} is the piezoelectric coefficient, and ε_0 and ε_r are the vacuum dielectric constant and the relative dielectric constant in the normal direction, respectively. d_{33} can be determined

according to equation 2[35]:

$$d_{33} = \frac{A - A_1}{V - V_1} \quad (2)$$

Where A_1 and V_1 represent the amplitude and voltage at the intersection of the loop, respectively. A and V represent their respective values at different points of the loop.

In most cases, the higher the d_{33} value, the better the piezocatalytic performance. But based on PFM analysis (Fig. 4b and Fig. S8), it was verified that the d_{33} of BMO were higher than that of BMO-0.1BTO heterojunction. However, this result does not align with the observed trend in piezocatalytic H_2 production performance (BMO-0.1BTO heterojunction>BMO). Therefore, it can be inferred that the high piezocatalytic H_2 production performance of BMO-0.1BTO heterojunction relative to pristine BMO may be not due to the increase in piezoelectricity in this work. Similar phenomena have been reported in other literature[51].

Broadly speaking, although a large number of works have illustrated that increasing the d_{33} value of piezoelectric materials is positively correlated with improving the piezocatalytic or piezo-photocatalytic performance of heterojunction catalytic materials, the author believes that this relationship is only applicable to semiconductor piezocatalytic or piezo-photocatalytic materials with the same or similar properties[52-56]. It does not apply to semiconductor catalytic materials with completely different properties, that is, heterojunction systems. For similar substances with similar physicochemical properties, the d_{33} value may play a significant role in exploring the mechanism of enhanced catalytic performance. For example, Hailong Jiang et al. studied two UiO-66 (Zr) and UiO-66 (Hf) materials with very similar properties, and they used the value of d_{33} to unveil the mechanism of improved piezo-photocatalytic performance, which is very reasonable at this time[57]. However, for heterojunction systems, the catalytic performance may be affected by other factors, such as the electronic structure, surface properties, specific surface area and the recombination rate of carriers in material, and

the d_{33} value can only be used as a reference. Therefore, the author believes that it is not practical to focus on the d_{33} value of the material alone to explain the mechanism in the piezocatalytic and piezo-photocatalytic heterojunction systems. Instead, it is more important to pay attention to the separation efficiency of carriers and other factors related to the heterojunction interface. This comprehensive approach is expected to improve the understanding of the mechanism of piezoelectric/piezoelectric photocatalysis, thereby providing strong support for the design and development of more efficient catalytic materials.

Additionally, the optical properties of BMO, BTO and BMO-0.1BTO heterojunction piezocatalysts were obtained using UV-vis-NIR diffuse reflectance spectroscopy (DRS) measurements. As exhibited in Fig. 4d, the maximum absorption wavelength of the BMO-0.1BTO heterojunction sample hardly shifted compared to the BMO sample. According to the Tauc diagram, the bandgap value is precisely determined by equation 3[35]:

$$(\alpha h\upsilon)^n = A\left(h\upsilon - E_g\right) \quad (3)$$

Where, α, h, ν, A, n, E_g represent the absorption coefficient, Planck constant, light frequency, A constant, semiconductor transition type; The indirect bandgap semiconductor is 0.5 and the direct bandgap semiconductor is 2.

The key difference between direct and indirect bandgap semiconductors is the efficiency of the electronic transition. Direct bandgap semiconductor materials allow efficient electronic transitions by emitting or absorbing photons. In contrast, indirect bandgap semiconductor materials involve additional momentum-conservation steps, making them less efficient at luminescence or absorption. In general, BMO is considered as an indirect bandgap semiconductor. BTO is regarded as a direct bandgap semiconductor. Hence, the indirect optical bandgap of BMO and the direct optical bandgap values of BTO were calculated to be about 2.13 and 3.18 eV, respectively (Fig. 4e-f). Additionally, Mott-Schottky (M-S) curves were used to further study the bandgap positions of BMO and BTO. The intersection of the linear part of

the curve with the X-axis provides direct information about the flat band potential positions.

As exhibited in Fig. 4g-h, according to equation 4, taking y as 0, the flat-band potential of BMO and BTO relative to Ag/AgCl electrode was calculated to be nearly -0.56 and -1.06 V, respectively. Equation 4 is as follows[58]:

$$\frac{1}{C^2} = \frac{2}{A^2 e \varepsilon_r \varepsilon_0 N_d}\left(V - V_{fb} - \frac{kT}{e}\right) \quad (4)$$

Where, C represents the specific capacity, A represents the effective surface area, ε_r and ε_0 represent the dielectric constant and vacuum permittivity of the catalyst, e represents the basic charge, N_d represents the carrier concentration of the catalyst, V represents the applied potential, V_{fb} represents the flat-band potential, k represents the Boltzmann constant, and T represents the absolute temperature.

The flat-band potential was utilized to refer to the Fermi level (E_f) position, so the V_{fb} Vs NHE of BMO and BTO can be calculated as approximately -0.36 and -0.86 V, respectively (V_{fb} Vs normal hydrogen electrode (NHE) = $E_{Ag/AgCl}$ + 0.2 V). In general, the conduction band (CB) minimum values are about 0-0.3 V higher than the E_f of n-type semiconductors. Therefore, the CB potential for BMO and BTO was calculated to be nearly -0.66 and -1.16 eV, respectively. Meanwhile, the valence band (VB) maximum values is precisely determined by equation 5:

$$E_{VB} = E_g + E_{CB} \quad (5)$$

Where E_g, E_{VB} and E_{CB} represent the band gap, valence band and conduction band position.

The VB maximum values for BMO and BTO were determined to be approximately 1.47 and 2.02 eV, respectively (Fig. 4i). Hence, we can conclude that the band positions of BMO and BTO are suitable in terms of meeting the reduction potential requirements for reducing H^+ to H_2.

In addition, the energy band structures of MCC, STO, ZnO and CdS were also analyzed through the above series of characterization (Fig. S41-S56). Among them, the CB minimum

values of MCC, STO, ZnO and CdS were calculated as -0.61, -1.55, -0.76 and -1.62 eV, respectively, while the VB maximum values were determined to be 2.30, 1.73, 2.54 and 0.62 eV, respectively. The band position of these materials can meet the requirements of hydrogen production potential.

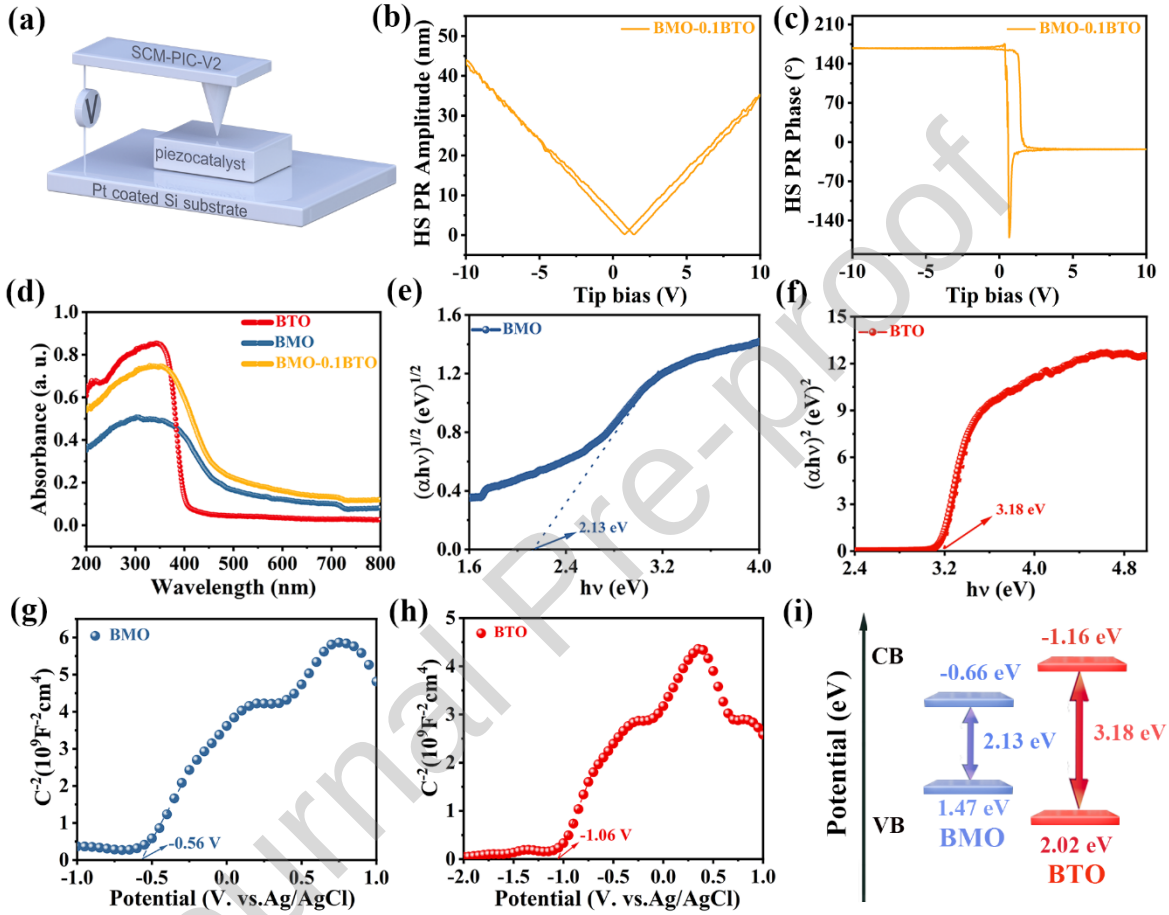

Fig. 4. (a) Schematic diagram of PFM test. (b) Amplitude-voltage curve of BMO-0.1BTO heterojunction. (c) Phase curve of BMO-0.1BTO heterojunction. (d) UV-visible diffuse reflectance spectra of BMO, BTO and BMO-0.1BTO heterojunction. (e-f) Tauc plots of BMO and BTO. (g-h) Mot-Schottky curve for BMO and BTO. (i) Band structure diagram of BMO and BTO (Vs. NHE).

As mentioned in the previous section, the piezocatalytic performance of heterojunctions should be more dependent on the separation efficiency of piezocarriers. Hence, a series of electrochemical and piezoelectrochemical characterization experiments were carried out to investigate the separation and transfer capabilities of piezocarriers. As exhibited in Fig. 5a, it

was evident that the BMO-0.1BTO heterojunction displayed a higher transient piezoelectric current response compared to both BMO and BTO upon the introduction of ultrasonic vibration. This observation suggested an improved capability to suppress the recombination rates of piezocarriers in the BMO-0.1BTO heterojunction. In addition, electrochemical impedance spectroscopy (EIS) plots were performed to investigate the influence of heterojunction construction on separation and transfer efficiency of piezocarriers. As presented in Fig. 5b, it was evident that the EIS arc radius of the BMO-0.1BTO heterojunction was significantly smaller compared to those of BMO and BTO. This observation indicated that the transfer efficiency of piezocarriers was enhanced in the BMO-0.1BTO heterojunction. In addition, the linear sweep voltammetry (LSV) characterization was conducted to deeply reveal the charge carrier's migration and separation properties of piezocatalysts (Fig. S57). The results showed that BMO-0.1BTO heterojunction had a lower electrocatalytic H_2 production potential than that of BMO and BTO at the same current density. Therefore, the piezocatalytic H_2 production reaction was easier to occur. The combination of PFM, transient piezocurrent, and EIS test results validated the idea that a higher d_{33} value is merely a reference point for superior piezocatalytic performance in heterojunction. However, greater emphasis should be placed on the separation efficiency of piezocarriers.

Building upon the comprehensive investigation of bandgap structure and findings obtained from various electrochemical characterization experiments, we have proposed a plausible Type-I transfer mechanism to explain the enhanced piezocatalytic H_2 production performance in the BMO-BTO heterojunctions (Fig. 5c-d). Since both BMO and BTO belong to n-type piezoelectric semiconductor materials, the energy level of Fermi energy (E_f) for both materials is approximately 0.3 eV lower than the conduction band (CB). The energy difference between the E_f and the vacuum level (V_{ac}) is defined as the work function (W). Here, W_1 and W_2 were used to represent the respective work functions of BMO and BTO, respectively. The BMO and

BTO are both dielectric materials with electrical polarity (dipole moment>0), therefore they can produce a piezoelectric effect when subjected to external mechanical forces. During the piezocatalysis process, an inherent piezoelectric field within the BTO can be generated by ultrasonic vibration, which promoted the movement of charge carriers in opposite directions. Nevertheless, due to the energy level discrepancy between the CB of BTO and the VB of BMO, the excited electrons in the CB of BTO were inclined to move to the CB of BMO with a lower energy level, and the holes in the VB of BTO were likely to shift to the VB of BMO. Afterwards, numerous carriers accumulate in the CB and VB of BMO, and electrons and holes were separated and transported to the active sites. In an aqueous environment, H^+ can be reduced by electrons to generate H_2. The sacrificial agent MeOH reacted with holes, enhancing the separation efficiency of the piezoelectric carriers. These intricate processes ultimately synergized to realize exceptional piezocatalytic H_2 production performance.

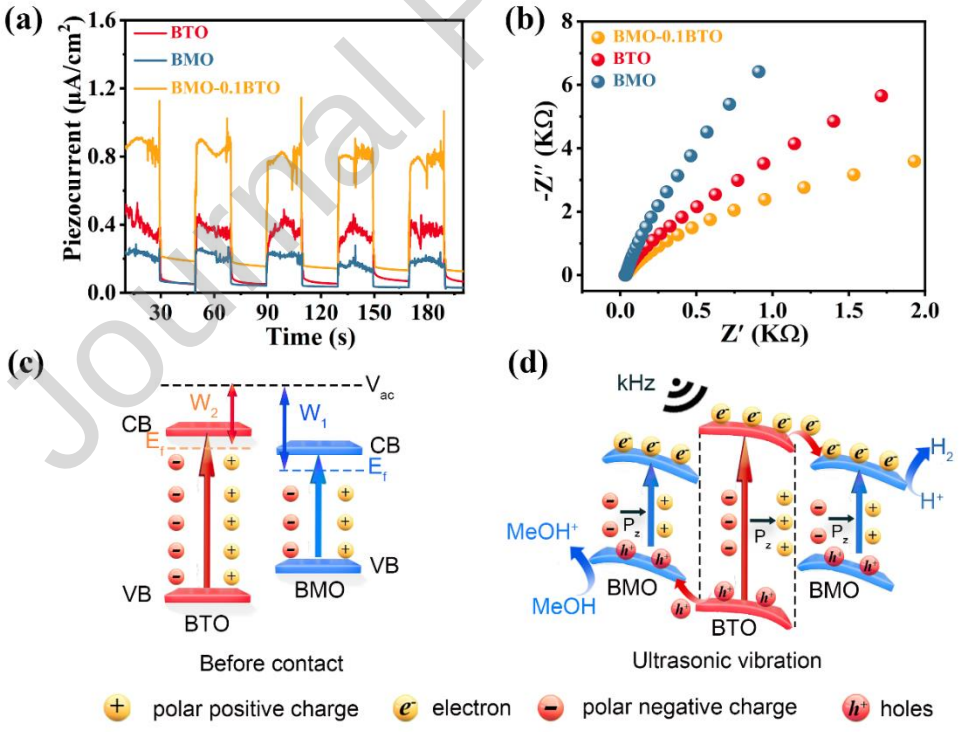

Fig. 5. (a) Transient piezoelectric current response diagrams of BMO, BTO and BMO-0.1BTO heterojunction. (b) EIS Nyquist plots of BMO, BTO and BMO-0.1BTO heterojunction. (c) Piezocatalytic H_2 production mechanism of BMO-BTO Type-I heterojunction.

4. Conclusion

To summarize, we had successfully synthesized BMO-BTO heterojunctions materials by a one-step solvothermal strategy, and applied them to piezocatalytic H_2 production reaction for the first time. The piezocatalytic H_2 production rates of pristine BMO and BTO can reach up to only 16.36 and 34.16 μmol/g/h, respectively. However, when they formed Type-I heterojunction, the piezocatalytic H_2 production rate significantly increased. In particular, in the BMO-0.1BTO Type-I heterojunction containing the optimal BTO loading amount, the piezocatalytic H_2 production rate was 9.33 and 4.47 times higher than that of BMO or BTO alone, respectively. Moreover, the BMO was combined with various conventional piezoelectric semiconductor materials to create heterojunctions, also resulting in similarly remarkable piezocatalytic H_2 production capabilities. The enhanced H_2 production performacne can be ascribed to the BIEF in Type-I heterojunction effectively improved the separation and transfer efficiency of piezocarriers, rather than an increase in piezoelectricity. In a word, this study provides a broad application prospect for future utilization of BMO-based heterojunction materials in efficiently converting mechanical energy into chemical energy.

Acknowledgements

The authors thank Shiyanjia Lab (www.shiyanjia.com) for the support of XPS, BET, TG and PFM tests. This work was supported by the National Natural Science Foundation of China (Nos. 22101105, 52071171, 52202248), the Research Fund for the Doctoral Program of Liaoning Province (2021-BS-086, 2022-BS-210), Liaoning BaiQianWan Talents Program (LNBQW2018B0048), Shenyang Science and Technology Project (21-108-9-04), Australian Research Council (ARC) through Future Fellowship (FT210100298, FT210100806), Discovery Project (DP220100603), Linkage Project (LP210100467, LP210200504,

LP210200345, LP220100088), and Industrial Transformation Training Centre (IC180100005) schemes, and the Australian Government through the Cooperative Research Centres Projects (CRCPXIII000077).

Reference

[1] Y.-T. Liu, M.-Y. Lu, T.-P. Perng, L.-J. Chen, Plasmonic enhancement of hydrogen production by water splitting with CdS nanowires protected by metallic TiN overlayers as highly efficient photocatalysts, Nano Energy. 89 (2021), 106407, http://dx.doi.org/https://doi.org/10.1016/j.nanoen.2021.106407.

[2] S. Zhang, K. Wang, F. Li, S.-H. Ho, Structure-mechanism relationship for enhancing photocatalytic H_2 production, Int. J. Hydrogen Energy. 47 (2022), 37517-37530, http://dx.doi.org/https://doi.org/10.1016/j.ijhydene.2021.10.139.

[3] Y. Zhao, S. Zhao, H. Huang, Z. Liu, X. Cheng, G. Dawson, Enhanced photocatalytic hydrogen production by the formation of TiNT-BN bonds, Appl. Surf. Sci. 623 (2023), 157005, http://dx.doi.org/https://doi.org/10.1016/j.apsusc.2023.157005.

[4] F. Qiu, Z. Han, J.J. Peterson, M.Y. Odoi, K.L. Sowers, T.D. Krauss, Photocatalytic Hydrogen Generation by CdSe/CdS Nanoparticles, Nano Lett. 16 (2016), 5347-5352, http://dx.doi.org/10.1021/acs.nanolett.6b01087.

[5] H. Long, D. Gao, P. Wang, X. Wang, F. Chen, H. Yu, Amorphization-induced reverse electron transfer in NiB cocatalyst for boosting photocatalytic H_2 production, Appl. Catal., B. 340 (2024), 123270, http://dx.doi.org/https://doi.org/10.1016/j.apcatb.2023.123270.

[6] W. Huang, Q. He, Y. Hu, Y. Li, Molecular Heterostructures of Covalent Triazine Frameworks for Enhanced Photocatalytic Hydrogen Production, Angew. Chem., Int. Ed. 58 (2019), 8676-8680, http://dx.doi.org/https://doi.org/10.1002/anie.201900046.

[7] M.Z. Rahman, F. Raziq, H. Zhang, J. Gascon, Key Strategies for Enhancing H2 Production in Transition Metal Oxide Based Photocatalysts, Angew. Chem., Int. Ed. (2023), e202305385, http://dx.doi.org/https://doi.org/10.1002/anie.202305385.

[8] C. Hu, S. Tu, N. Tian, T. Ma, Y. Zhang, H. Huang, Photocatalysis Enhanced by External Fields, Angew. Chem., Int. Ed. 60 (2021), 16309-16328, http://dx.doi.org/https://doi.org/10.1002/anie.202009518.

[9] S. Xiong, R. Tang, D. Gong, Y. Deng, J. Zheng, L. Li, Z. Zhou, L. Yang, L. Su, Environmentally-friendly carbon nanomaterials for photocatalytic hydrogen production, Chin. J. Catal. 43 (2022), 1719-1748, http://dx.doi.org/https://doi.org/10.1016/S1872-2067(21)63994-3.

[10] X. Zheng, Y. Song, Y. Liu, Y. Yang, D. Wu, Y. Yang, S. Feng, J. Li, W. Liu, Y. Shen, X. Tian, $ZnIn_2S_4$-based photocatalysts for photocatalytic hydrogen evolution via water splitting, Coord. Chem. Rev. 475 (2023), 214898, http://dx.doi.org/https://doi.org/10.1016/j.ccr.2022.214898.

[11] S. Cao, J. Yu, Carbon-based H_2-production photocatalytic materials, J. Photochem. Photobiol., C. 27 (2016), 72-99, http://dx.doi.org/https://doi.org/10.1016/j.jphotochemrev.2016.04.002.

[12] Y. Yang, C. Zhou, W. Wang, W. Xiong, G. Zeng, D. Huang, C. Zhang, B. Song, W. Xue, X. Li, Z. Wang, D. He, H. Luo, Z. Ouyang, Recent advances in application of transition metal phosphides for photocatalytic hydrogen production, Chem. Eng. J. 405 (2021), 126547, http://dx.doi.org/https://doi.org/10.1016/j.cej.2020.126547.

[13] F. Zhang, Q. Wang, Redox-mediated electrocatalytic and photocatalytic hydrogen production, Curr. Opin. Electrochem. 35 (2022), 101097, http://dx.doi.org/https://doi.org/10.1016/j.coelec.2022.101097.

[14] M. Kuang, W. Huang, C. Hegde, W. Fang, X. Tan, C. Liu, J. Ma, Q. Yan, Interface engineering in transition metal carbides for electrocatalytic hydrogen generation and nitrogen fixation, Mater. Horiz. 7 (2020), 32-53, http://dx.doi.org/10.1039/C9MH01094G.

[15] K. Veeramani, G. Janani, J. Kim, S. Surendran, J. Lim, S.C. Jesudass, S. Mahadik, H. lee, T.-H. Kim, J.K. Kim, U. Sim, Hydrogen and value-added products yield from hybrid water electrolysis: A critical review on recent developments, Renewable Sustainable Energy Rev. 177 (2023), 113227, http://dx.doi.org/https://doi.org/10.1016/j.rser.2023.113227.

[16] W. Zhu, Z. Huang, M. Zhao, R. Huang, Z. Wang, H. Liang, Hydrogen production by electrocatalysis using the reaction of acidic oxygen evolution: a review, Environ. Chem. Lett. 20 (2022), 3429-3452, http://dx.doi.org/10.1007/s10311-022-01454-5.

[17] W. Tian, J. Han, L. Wan, N. Li, D. Chen, Q. Xu, H. Li, J. Lu, Enhanced piezocatalytic activity in ion-doped SnS_2 via lattice distortion engineering for BPA degradation and hydrogen production, Nano Energy. 107 (2023), 108165, http://dx.doi.org/https://doi.org/10.1016/j.nanoen.2023.108165.

[18] Y. Du, T. Lu, X. Li, Y. Liu, W. Sun, S. Zhang, Z. Cheng, High-efficient piezocatalytic hydrogen evolution by centrosymmetric $Bi_2Fe_4O_9$ nanoplates, Nano Energy. 104 (2022), 107919, http://dx.doi.org/https://doi.org/10.1016/j.nanoen.2022.107919.

[19] X. Xu, L. Xiao, Z. Wu, Y. Jia, X. Ye, F. Wang, B. Yuan, Y. Yu, H. Huang, G. Zou, Harvesting vibration energy to piezo-catalytically generate hydrogen through Bi_2WO_6 layered-perovskite, Nano Energy. 78 (2020), 105351, http://dx.doi.org/https://doi.org/10.1016/j.nanoen.2020.105351.

[20] Q. Liu, F. Zhan, X. Luo, Q. Yi, Z. Xiao, D. Zhai, J. Huang, Y. Zhang, H. Luo, D. Zhang, C.R. Bowen, A $(Bi_2O_2)^{2+}$ layer as a significant carrier generator and transmission channel in $CaBi_2Nb_2O_9$ platelets for enhanced piezo-photo-catalytic performance, Nano Energy. 108 (2023), 108252, http://dx.doi.org/https://doi.org/10.1016/j.nanoen.2023.108252.

[21] C.-C. Jin, D.-M. Liu, L.-X. Zhang, An Emerging Family of Piezocatalysts: 2D Piezoelectric Materials, Small. (2023), 2303586, http://dx.doi.org/https://doi.org/10.1002/smll.202303586.

[22] X. Liu, M. Wang, Y. Zhou, T. Li, H. Duan, J. Li, L. Wang, Y. Li, S. Yang, J. Wu, C. Wang, X. Feng, F. Li, Ultrahigh Piezocatalytic Performance of Perovskite Ferroelectric Powder via Oxygen Vacancy Engineering, Small. (2023), 2303129, http://dx.doi.org/https://doi.org/10.1002/smll.202303129.

[23] P. Hu, Y. Xu, Y. Lei, J. Yuan, R. Lei, R. Hu, J. Chen, D. Xu, S. Zhang, P. Liu, X. Zhang, X. Qiu, W. Feng, Piezoelectric nanofoams with the interlaced ultrathin graphene confining Zn–N–C dipoles for efficient piezocatalytic H_2 evolution under low-frequency vibration, J. Energy Chem. 69 (2022), 115-122, http://dx.doi.org/https://doi.org/10.1016/j.jechem.2022.01.009.

[24] X. Lu, T. Shan, L. Deng, M. Li, X. Pan, X. Yang, X. Zhao, M.-Q. Yang, Facile synthesis of hierarchical CdS nanoflowers for efficient piezocatalytic hydrogen evolution, Dalton Trans. 52 (2023), 13426-13434, http://dx.doi.org/10.1039/D3DT02328A.

[25] X. Xiong, Y. Wang, J. Ma, Y. He, J. Huang, Y. Feng, C. Ban, L.-Y. Gan, X. Zhou, Oxygen vacancy engineering of zinc oxide for boosting piezo-electrocatalytic hydrogen evolution, Appl. Surf. Sci. 616 (2023), 156556, http://dx.doi.org/https://doi.org/10.1016/j.apsusc.2023.156556.

[26] R. Lei, F. Gao, J. Yuan, C. Jiang, X. Fu, W. Feng, P. Liu, Free layer-dependent piezoelectricity of oxygen-doped MoS_2 for the enhanced piezocatalytic hydrogen evolution from pure water, Appl. Surf. Sci. 576 (2022), 151851, http://dx.doi.org/https://doi.org/10.1016/j.apsusc.2021.151851.

[27] D. Liu, X. Sun, L. Tan, J. Zhang, C.-C. Jin, F. Wang, High-performance piezocatalytic hydrogen evolution by $(Bi_{0.5}Na_{0.5})TiO_3$ cubes decorated with cocatalysts, Ceram. Int. 49 (2023), 20343-20350, http://dx.doi.org/https://doi.org/10.1016/j.ceramint.2023.03.158.

[28] B. Wang, Q. Zhang, J. He, F. Huang, C. Li, M. Wang, Co-catalyst-free large ZnO single crystal for high-efficiency piezocatalytic hydrogen evolution from pure water, J. Energy Chem. 65 (2022), 304-311, http://dx.doi.org/https://doi.org/10.1016/j.jechem.2021.06.004.

[29] J. Wang, C. Hu, Y. Zhang, H. Huang, Engineering piezoelectricity and strain sensitivity in CdS to promote piezocatalytic hydrogen evolution, Chin. J. Catal. 43 (2022), 1277-1285, http://dx.doi.org/https://doi.org/10.1016/S1872-2067(21)63976-1.

[30] C. Hu, F. Chen, Y. Wang, N. Tian, T. Ma, Y. Zhang, H. Huang, Exceptional Cocatalyst-Free Photo-Enhanced Piezocatalytic Hydrogen Evolution of Carbon Nitride Nanosheets from Strong In-Plane Polarization, Adv. Mater. 33 (2021), 2101751, http://dx.doi.org/https://doi.org/10.1002/adma.202101751.

[31] S. Zhao, M. Liu, Y. Zhang, Z. Zhao, Q. Zhang, Z. Mu, Y. Long, Y. Jiang, Y. Liu, J. Zhang, S. Li, X. Zhang, Z. Zhang, Harvesting mechanical energy for hydrogen generation by piezoelectric metal–organic frameworks, Mater. Horiz. 9 (2022), 1978-1983, http://dx.doi.org/10.1039/D1MH01973B.

[32] M. Banoo, R.S. Roy, M. Bhakar, J. Kaur, A. Jaiswal, G. Sheet, U.K. Gautam, Bi_4TaO_8Cl as a New Class of Layered Perovskite Oxyhalide Materials for Piezopotential Driven Efficient Seawater Splitting, Nano Lett. 22 (2022), 8867-8874, http://dx.doi.org/10.1021/acs.nanolett.2c02900.

[33] Y. Long, H. Xu, J. He, C. Li, M. Zhu, Piezoelectric polarization of BiOCl via capturing mechanical energy for catalytic H_2 evolution, Surf. Interfaces. 31 (2022), 102056, http://dx.doi.org/https://doi.org/10.1016/j.surfin.2022.102056.

[34] P. Hao, Y. Cao, X. Ning, R. Chen, J. Xie, J. Hu, Z. Lu, A. Hao, Rational design of CdS/BiOCl S-scheme heterojunction for effective boosting piezocatalytic H_2 evolution and pollutants degradation performances, J. Colloid Interface Sci. 639 (2023), 343-354, http://dx.doi.org/https://doi.org/10.1016/j.jcis.2023.02.075.

[35] C. Wang, C. Hu, F. Chen, H. Li, Y. Zhang, T. Ma, H. Huang, Polar Layered Bismuth-Rich Oxyhalide Piezoelectrics $Bi_4O_5X_2$ (X=Br, I): Efficient Piezocatalytic Pure Water Splitting and Interlayer Anion-Dependent Activity, Adv. Funct. Mater. 33 (2023), 2301144, http://dx.doi.org/https://doi.org/10.1002/adfm.202301144.

[36] D. Liu, J. Zhang, L. Tan, C. Jin, M. Li, B. Chen, G. Zhang, Y. Zhang, F. Wang, Enhanced piezocatalytic hydrogen evolution performance of bismuth vanadate by the synergistic effect of facet engineering and cocatalyst engineering, J. Colloid Interface Sci. 646 (2023), 159-166, http://dx.doi.org/https://doi.org/10.1016/j.jcis.2023.05.040.

[37] X. Zhang, X. Wang, G. Li, L. Wang, J. Huang, A. Meng, Z. Li, Construction of electron donor–acceptor Z-scheme heterojunction for boosting photocatalytic H_2 production, Appl. Surf. Sci. 635 (2023), 157625, http://dx.doi.org/https://doi.org/10.1016/j.apsusc.2023.157625.

[38] G. Liao, C. Li, B. Fang, Donor-acceptor organic semiconductor heterojunction nanoparticles for efficient photocatalytic H_2 evolution, Matter. 5 (2022), 1635-1637, http://dx.doi.org/https://doi.org/10.1016/j.matt.2022.05.001.

[39] W. Ge, J. Song, S. Deng, K. Liu, P. Yang, Construction of Z-scheme $CoFe_2O_4$@$ZnIn_2S_4$ p-n heterojunction for enhanced photocatalytic hydrogen production, Sep. Purif. Technol. 328 (2024), 125059, http://dx.doi.org/https://doi.org/10.1016/j.seppur.2023.125059.

[40] F. Fu, H. Shen, W. Xue, Y. Zhen, R.A. Soomro, X. Yang, D. Wang, B. Xu, R. Chi, Alkali-assisted synthesis of direct Z-scheme based Bi_2O_3/Bi_2MoO_6 photocatalyst for highly efficient photocatalytic degradation of phenol and hydrogen evolution reaction, J. Catal. 375 (2019), 399-409, http://dx.doi.org/https://doi.org/10.1016/j.jcat.2019.06.033.

[41] C. Yang, Y. Zhang, F. Yue, R. Du, T. Ma, Y. Bian, R. Li, L. Guo, D. Wang, F. Fu, Co doping regulating electronic structure of Bi_2MoO_6 to construct dual active sites for photocatalytic nitrogen fixation, Appl. Catal., B. 338 (2023), 123057, http://dx.doi.org/https://doi.org/10.1016/j.apcatb.2023.123057.

[42] T. Ma, C. Yang, L. Guo, R.A. Soomro, D. Wang, B. Xu, F. Fu, Refining electronic properties of Bi_2MoO_6 by In-doping for boosting overall nitrogen fixation via relay catalysis, Appl. Catal., B. 330 (2023), 122643, http://dx.doi.org/https://doi.org/10.1016/j.apcatb.2023.122643.

[43] X. Zhou, F. Yan, S. Wu, B. Shen, H. Zeng, J. Zhai, Remarkable Piezophoto Coupling Catalysis Behavior of BiOX/$BaTiO_3$ (X = Cl, Br, $Cl_{0.166}Br_{0.834}$) Piezoelectric Composites, Small. 16 (2020), 2001573, http://dx.doi.org/https://doi.org/10.1002/smll.202001573.

[44] J. Guo, L. Shi, J. Zhao, Y. Wang, K. Tang, W. Zhang, C. Xie, X. Yuan, Enhanced visible-light photocatalytic activity of Bi_2MoO_6 nanoplates with heterogeneous Bi_2MoO_{6-x}@Bi_2MoO_6 core-shell structure, Appl. Catal., B. 224 (2018), 692-704, http://dx.doi.org/https://doi.org/10.1016/j.apcatb.2017.11.030.

[45] Q. Xiao, L. Chen, Y. Xu, W. Feng, X. Qiu, Impact of oxygen vacancy on piezo-photocatalytic catalytic activity of barium titanate, Appl. Surf. Sci. 619 (2023), 156794, http://dx.doi.org/https://doi.org/10.1016/j.apsusc.2023.156794.

[46] W.W. Lee, W.-H. Chung, W.-S. Huang, W.-C. Lin, W.-Y. Lin, Y.-R. Jiang, C.-C. Chen, Photocatalytic activity and mechanism of nano-cubic barium titanate prepared by a hydrothermal method, J. Taiwan Inst. Chem. Eng. 44 (2013), 660-669, http://dx.doi.org/https://doi.org/10.1016/j.jtice.2013.01.005.

[47] H. Gao, Y. Zhang, H. Xia, X. Zhu, X. Mao, W. Zhao, S. Miao, M. Shi, In situ generation of H_2O_2 over Ce-doped $BaTiO_3$ catalysts for enhanced piezo-photocatalytic degradation of pollutants in aqueous solution, Colloids Surf., A. 663 (2023), 131030, http://dx.doi.org/https://doi.org/10.1016/j.colsurfa.2023.131030.

[48] Y. Zhang, L. Guo, Y. Wang, T. Wang, T. Ma, Z. Zhang, D. Wang, B. Xu, F. Fu, In-situ anion exchange based Bi_2S_3/OV-Bi_2MoO_6 heterostructure for efficient ammonia production: A synchronized approach to strengthen NRR and OER reactions, J. Mater. Sci. Technol. 110 (2022), 152-160, http://dx.doi.org/https://doi.org/10.1016/j.jmst.2021.09.009.

[49] T. Yan, Q. Yan, X. Wang, H. Liu, M. Li, S. Lu, W. Xu, M. Sun, Facile fabrication of heterostructured g-C_3N_4/Bi_2MoO_6 microspheres with highly efficient activity under visible light irradiation, Dalton Trans. 44 (2015), 1601-1611, http://dx.doi.org/10.1039/C4DT02127D.

[50] D. Wang, H. Shen, L. Guo, C. Wang, F. Fu, Porous BiOBr/Bi_2MoO_6 Heterostructures for Highly Selective Adsorption of Methylene Blue, ACS Omega. 1 (2016), 566-577, http://dx.doi.org/10.1021/acsomega.6b00160.

[51] O.S. Ekande, M. Kumar, New insight on interfacial charge transfer at graphitic carbon nitride/sodium niobate heterojunction under piezoelectric effect for the generation of reactive oxygen species, J. Colloid Interface Sci. 651 (2023), 477-493, http://dx.doi.org/https://doi.org/10.1016/j.jcis.2023.07.189.

[52] W. Liu, P. Wang, Y. Ao, J. Chen, X. Gao, B. Jia, T. Ma, Directing Charge Transfer in a Chemical-Bonded $BaTiO_3$@ReS_2 Schottky Heterojunction for Piezoelectric Enhanced Photocatalysis, Adv. Mater. 34 (2022), 2202508, http://dx.doi.org/https://doi.org/10.1002/adma.202202508.

[53] R. Xiong, Y. Song, K. Li, Y. Xiao, B. Cheng, S. Lei, A novel 1D/2D core/shell CdS@SnS_2 heterostructure for efficient piezocatalytic hydrogen evolution and pollutant degradation, J. Mater. Chem. A. 11 (2023), 18398-18408, http://dx.doi.org/10.1039/D3TA03003B.

[54] J. Long, T. Ren, J. Han, N. Li, D. Chen, Q. Xu, H. Li, J. Lu, Heterostructured $BiFeO_3$@CdS nanofibers with enhanced piezoelectric response for efficient piezocatalytic degradation of organic pollutants, Sep. Purif. Technol. 290 (2022), 120861, http://dx.doi.org/https://doi.org/10.1016/j.seppur.2022.120861.

[55] Y. Cheng, J. Chen, P. Wang, W. Liu, H. Che, X. Gao, B. Liu, Y. Ao, Interfacial engineering boosting the piezocatalytic performance of Z-scheme heterojunction for carbamazepine degradation: Mechanism, degradation pathway and DFT calculation, Appl. Catal., B. 317 (2022), 121793, http://dx.doi.org/https://doi.org/10.1016/j.apcatb.2022.121793.

[56] M.-L. Xu, M. Lu, G.-Y. Qin, X.-M. Wu, T. Yu, L.-N. Zhang, K. Li, X. Cheng, Y.-Q. Lan, Piezo-Photocatalytic Synergy in $BiFeO_3$@COF Z-Scheme Heterostructures for High-Efficiency Overall Water Splitting, Angew. Chem., Int. Ed. 61 (2022), e202210700, http://dx.doi.org/https://doi.org/10.1002/anie.202210700.

[57] C. Zhang, D. Lei, C. Xie, X. Hang, C. He, H.-L. Jiang, Piezo-Photocatalysis over Metal–Organic Frameworks: Promoting Photocatalytic Activity by Piezoelectric Effect, Adv. Mater. 33 (2021), 2106308, http://dx.doi.org/https://doi.org/10.1002/adma.202106308.

[58] S. Li, Z. Zhao, J. Li, H. Liu, M. Liu, Y. Zhang, L. Su, A.I. Pérez-Jiménez, Y. Guo, F. Yang, Y. Liu, J. Zhao, J. Zhang, L.-D. Zhao, Y. Lin, Mechanically Induced Highly Efficient Hydrogen Evolution from Water over Piezoelectric SnSe nanosheets, Small. 18 (2022), 2202507, http://dx.doi.org/https://doi.org/10.1002/smll.202202507.

Graphical abstract

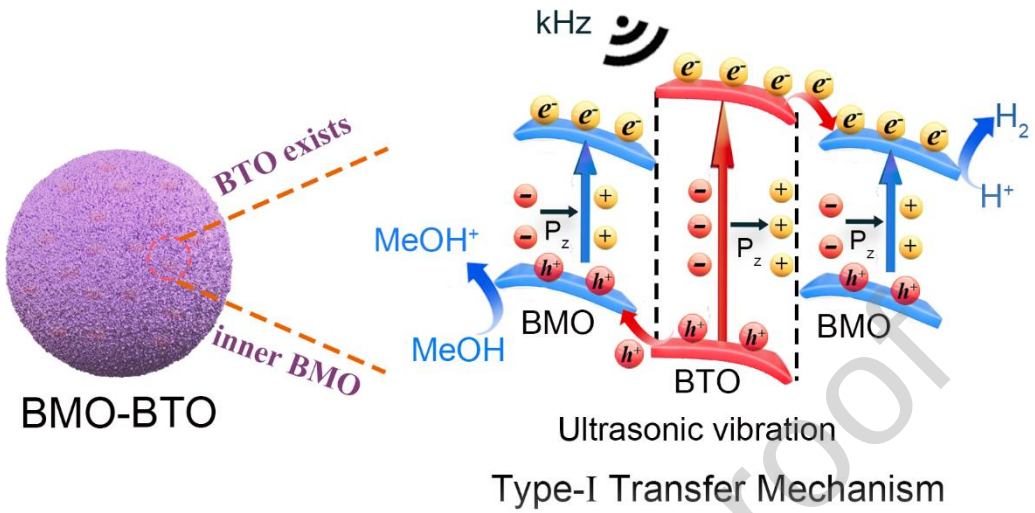

Bi_2MoO_6-$BaTiO_3$ (BMO-BTO) Type-I heterojunction piezocatalyst is successfully fabricated and applied for cocatalysts-free piezocatalytic H_2 production reaction. The enhanced piezocatalytic H_2 performance can be attributed to the established built-in electric field (BIEF) in heterojunction remarkably reduced the recombination rates of carriers, rather than an increase in piezoelectricity.

Declaration of interests

☒ The authors declare that they have no known competing financial interests or personal relationships that could have appeared to influence the work reported in this paper.

☐ The authors declare the following financial interests/personal relationships which may be considered as potential competing interests:

Highlights

- Highly efficient piezocatalysts of BMO-BTO Type-I heterojunctions were rationally designed.
- BMO-BTO Type-I heterojunctions owned excellent piezocatalytic H_2 production activity and stability.
- An innovative piezocatalytic mechanism of BMO-BTO Type-I heterojunctions was reasonablely elucidated.
- The enhanced H_2 production performance can be attributed to the new BIEF caused by the formation of Type-I heterojunction effectively improved the separation efficiency of carriers, rather than an increase in material piezoelectricity.